Materials Today • Volume xxx, Number xx • xxxx 2024

ELSEVIER

Ablation-resistant yttrium-modified high-entropy refractory metal silicide $(NbMoTaW)Si_2$ coating for oxidizing environments up to 2100 °C

Juan Kuang [a], Qianqian Wang [a,b], Zhe Jia [a,*], Guoming Yi [a], Bo Sun [a], Yiyuan Yang [a], Ligang Sun [c], Ping Zhang [d], Pengfei He [a], Yue Xing [a], Xiubing Liang [a,*], Yang Lu [e,*], Baolong Shen [a,*]

[a] School of Materials Science and Engineering, Jiangsu Key Laboratory for Advanced Metallic Materials, Southeast University, Nanjing 211189, China
[b] School of Materials Science and Engineering, Jiangsu Key Laboratory of Advanced Structural Materials and Application Technology, Nanjing Institute of Technology, Nanjing 211167, China
[c] School of Science, Harbin Institute of Technology, Shenzhen 518055, China
[d] School of Material Science and Physics, China University of Mining and Technology, Xuzhou 221116, China
[e] Department of Mechanical Engineering, The University of Hong Kong, Pokfulam Road, the Hong Kong Special Administrative Region of China

Refractory high-entropy alloys (RHEAs) are pivotal in ultra-high temperature applications, such as rocket nozzles, aerospace engines, and leading edges of hypersonic vehicles due to their exceptional mechanical ability to withstand severe thermal environments (in excess of 2000 °C). However, the selection of materials that satisfy the stringent criteria required for effective ablation resistance remains notably restricted. Here, a novel yttrium-modified high-entropy refractory metal silicide (Y-HERMS) coated on a refractory high-entropy NbMoTaW alloy is developed via pack cementation process. The developed Y-HERMS coating with sluggish diffusion effect demonstrates extraordinary ablation resistance, maintaining near-zero damage at sustained temperatures up to 2100 °C for a duration of 180 s, surpassing state-of-the-art high-performance silicide coatings. Such exceptional ultra-high ablation performance is primarily ascribed to the in-situ development of a high viscosity Si-Y-O oxide layer with increased thermal stability and the presence of high-melting $Y(Nb_{0.5}Ta_{0.5})O_4$ oxides as skeleton structure. Theoretical results elucidate that the Y-HERMS promotes the formation of SiO_2, which impedes the diffusion of O into metal silicide layer, synergistically contributing to the superior ablation resistance. These findings highlight the potential of utilizing high-entropy materials with excellent ablation resistance in extreme thermal environments.

Keywords: Refractory high-entropy alloy; High-entropy refractory metal silicide; Yttrium modification; Ultra-high temperature; Ablation resistance

Introduction

Future hypersonic aerospace vehicles promise revolutionary increases in transit speeds, presenting unprecedented engineering challenges. One of the most critical of these is the development of effective protective strategies for essential components, such as leading edges, combustors, and nose tips against severe oxidation and the extreme thermal scouring associated with heat fluxes exceeding 2,000 °C during flight [1,2]. Refractory high-entropy alloys (RHEAs), characterized by their constitution of multiple principal refractory metals and significant mixing entropy, are emerging as excellent candidates for such ultra-high temperature applications [3]. Within this class, NbMoTaW-based RHEAs have been recognized for their excep-

* Corresponding authors.
E-mail addresses: Jia, Z. (zhejia@seu.edu.cn), Liang, X. (liangxb_d@163.com), Lu, Y. (ylu1@hku.hk), Shen, B. (blshen@seu.edu.cn).

 https://doi.org/10.1016/j.mattod.2024.08.012

Please cite this article in press as: J. Kuang et al., Materials Today (2024), https://doi.org/10.1016/j.mattod.2024.08.012

tional high-temperature attributes, including yield strength, thermal stability, and resistance to softening [4]. Nevertheless, the suboptimal oxidation and ablation resistance at elevated temperatures compromises the mechanical integrity of NbMoTaW RHEAs, thus presenting a formidable barrier to their broader industrial deployment [5].

An alternative approach to protect RHEAs from oxidation and ablation is the application of oxidation and ablation resistant coatings on the surface of RHEAs [6,7]. Silicide coatings have shown exceptional oxidation performance at temperatures above 1200 °C, primarily due to the formation of a dense SiO_2 layer on the surface [8–10]. Encouraged by these findings, the scientific community has proceeded to explore the potential of enhanced silicide coatings through the strategic incorporation of additional elements, such as Ge [11], Ce [12], Y [13], Al [14], and B [15]. Among these modifying elements, Y as a rare earth element with unique electronic structure and reactive element effects, can significantly enhance the oxidation resistance of coatings by inhibiting the outward diffusion of metal ions, thus improving scale adhesion, and reducing oxidation rates [16]. *Wang et al.* reported that an appropriate amount of Y_2O_3 helped to strengthen the Si-O bonds in SiO_2 glass scale during oxidation, and then modified the oxidation resistance of the coating [17]. While prior research on Y-modified silicide coatings has predominantly concentrated on evaluating their oxidation behavior within the temperature bracket of 1300 to 1500 °C, scrutiny into their ablation resistance, particularly at exceedingly high temperatures, remains sparse. Observations indicate that the rapid volatilization of silicon-based oxides, such as SiO and SiO_2, can undermine the stability and integrity of the protective layer under extreme conditions that surpass 2100 °C for prolonged durations [18]. Consequently, fortifying the stability of the oxide layer is pivotal for the enhancement of the ablation resistance of silicide coatings. Given that the current generation of metal silicides may not meet the escalating demands of advanced applications, there is a pressing imperative to innovate and develop materials with improved capabilities.

In recent years, a shift in focus has been seen from conventional transition metal silicides (*e.g.*, $NbSi_2$, $MoSi_2$, WSi_2, $TaSi_2$, $HfSi_2$, and $CrSi_2$) to a new class of materials known as high-entropy refractory metal silicides (HERMS). HERMS, characterized by their composition of at least four different metal cations, have captured the attention of the research community owing to their impressive array of properties. These materials boast an exceptionally high-melting point and hardness, coupled with excellent thermal stability, which are desirable traits for applications requiring thermal management [19–24]. For instance, *Liu et al.* investigated the oxidation behavior of $(Mo_{0.2}W_{0.2}Cr_{0.2}Ta_{0.2}Nb_{0.2})Si_2$ at 500 °C for 300 h. The developed HERMS exhibits superior oxidation resistance compared to the pure $MoSi_2$ materials, which was ascribed to features of high entropy, sluggish diffusion and cocktail effects, suppressing generation of bulk metallic oxides and promoting the formation of an intact SiO_2 film during oxidation [25]. *Ye et al.* reported that $(Mo_{0.2}Nb_{0.2}Ta_{0.2}V_{0.2}W_{0.2})Si_2$ ceramics are stable at 800 and 1600 °C and exhibit better oxidation resistance than $MoSi_2$ without pest behavior between 500 and 1000 °C, owing to the sluggish diffusion and the selective oxidation of Si atoms [26]. Recognizing the exceptional antioxidant capabilities and high-temperature structural integrity of HERMS, the scientific community is increasingly acknowledging their immense potential in developing coatings that can resist high-temperature oxidation and ablation for refractory alloys [27,28]. Unlike the static conditions of isothermal oxidation, an ablation flame offers a more accurate representation of the severe operational environments encountered by hypersonic aircraft [29]. This dynamic setting introduces aggressive thermal shocks and material erosion due to high-velocity particles, which coatings must withstand to protect underlying structures. Therefore, advancing the ablation resistance of HERMS coatings is of critical importance. Despite this, research directed towards optimizing the ablation resistance of HERMS has been relatively scarce thus far. It is essential to explore the mechanisms of ablation resistance in HERMS and to develop coatings that can effectively safeguard materials against the extreme conditions experienced during high-speed flight.

In this study, a novel approach is introduced to enhance the ablation resistance of RHEAs by employing a solid-phase diffusion method combined with the halide activated pack cementation (HAPC) technique. This method is utilized to fabricate a Y-modified HERMS coating on a high-entropy NbMoTaW alloy. The developed HERMS coatings are subjected to rigorous testing using an ultra-high air plasma flame to simulate the extreme conditions encountered by materials on hypersonic aircraft. The Y-modified HERMS coating exhibits extraordinary ablation resistance at sustained temperatures reaching 2100 °C for 180 s, showcasing its potential as a protective layer for high-temperature applications. Post-ablation analysis of the HERMS coating reveals that the formation of $Y(Ta_{0.5}Nb_{0.5})O_4$ as microstructured skeleton within the oxide layer plays a pivotal role in enhancing the thermal stability and ablation performance of the Si-Y-O oxide layer. Density functional theory (DFT) calculations indicate that the presence of Y facilitates the diffusion of Si and is theoretically shown to strengthen the Si-O bonds, which in turn increases the viscosity of the SiO_2 glass. As a result of these modifications, the diffusion of O is impeded, thus further improving the oxidative and ablative resistance of the coating. This research presents a significant advancement in protective coating technology for RHEAs, providing a new pathway for the development of materials capable of withstanding the harsh thermal and oxidative environments experienced during high-speed flight.

Materials and methods

Materials

The primary alloy ingot of $Nb_{25}Mo_{25}Ta_{25}W_{25}$ (at.%) was prepared by magnetic levitation melting method with high purity elemental raw materials (>99.95 wt. %), and a 5 kg column-shaped ingot was cast. Specimens with dimensions of 6 mm × 6 mm × 3 mm and 32 mm × 16 mm × 5 mm were extracted from the ingot by wire-cutting for follow-up experiments. After being ground up to 1500-grit for each side with silicon carbide paper, the specimens were cleaned in an ultrasonic ethanol bath and then dried.

Please cite this article in press as: J. Kuang et al., Materials Today (2024), https://doi.org/10.1016/j.mattod.2024.08.012

Coating preparation

A halide activated pack cementation process was employed to prepare the unmodified and Y-modified silicide coating on the substrate alloy. The co-deposition filling cementation was achieved by using Si and Y_2O_3 as donor sources, Al_2O_3 powders as inert filler, and NaF as the halide activator. Pack powder mixtures with a nominal composition of 30Si–$x$$Y_2O_3$–5NaF–(65-$x$) Al_2O_3 (wt.%, x = 0, 2, 4, 6, 8) were weighted and mixed in a ball mill for 4 h. The pack powders were then placed around the substrates in a cylindrical alumina crucible and sealed with an alumina lid using silica sol binder. The loaded crucible was placed in an alumina tube furnace and the temperature was gradually increased to 1000 °C at a rate of 10 °C/min. The samples were held at this temperature for 12 h under Ar flow. The furnace was then cooled to room temperature at a rate of 5 °C/min. It has been reported previously that increasing the preparation temperature can accelerate the diffusion rate of silicon in the high-entropy alloy, resulting in defects such as cracks [27]. In this study, the temperature was reduced to obtain a denser and defect-free coating. After HAPC fabrication, the coated samples were ultrasonically rinsed to remove any residual powder mixtures on the surface.

Ablation test

We initially studied the coatings prepared with different Y_2O_3 contents, where the cross-sectional scanning electron microscope (SEM) images of these samples are shown in Fig. S1. Notably, the Y-modified HERMS with the Y_2O_3 content of 4 wt. % (denoted as Y4-HERMS) achieved a maximum thickness of approximately 58 μm, which is crucial for enhancing coating ablation resistance. To investigate the effect of Y modification on ablation resistance, subsequent studies would be focused on comparing the Y-free HERMS (denoted as Y0-HERMS) and Y4-HERMS samples.

The oxidation behavior of the samples was investigated over a broader temperature range (Fig. S2) using thermogravimetric analysis (TGA), while the oxidation kinetics at 1450 °C were studied through static oxidation experiments conducted in a high-temperature furnace (Fig. S3). The corresponding results and discussions are presented in Text S1.

The ablation behavior of samples was evaluated by air plasma flame system. The experimental setup is depicted in Fig. 1, where specimens measuring 32 mm × 16 mm × 5 mm were positioned vertically to the torch at a distance of 50 mm. The Ar and H_2 flow rates were set to be 85 and 16 slpm, respectively. To dynamically

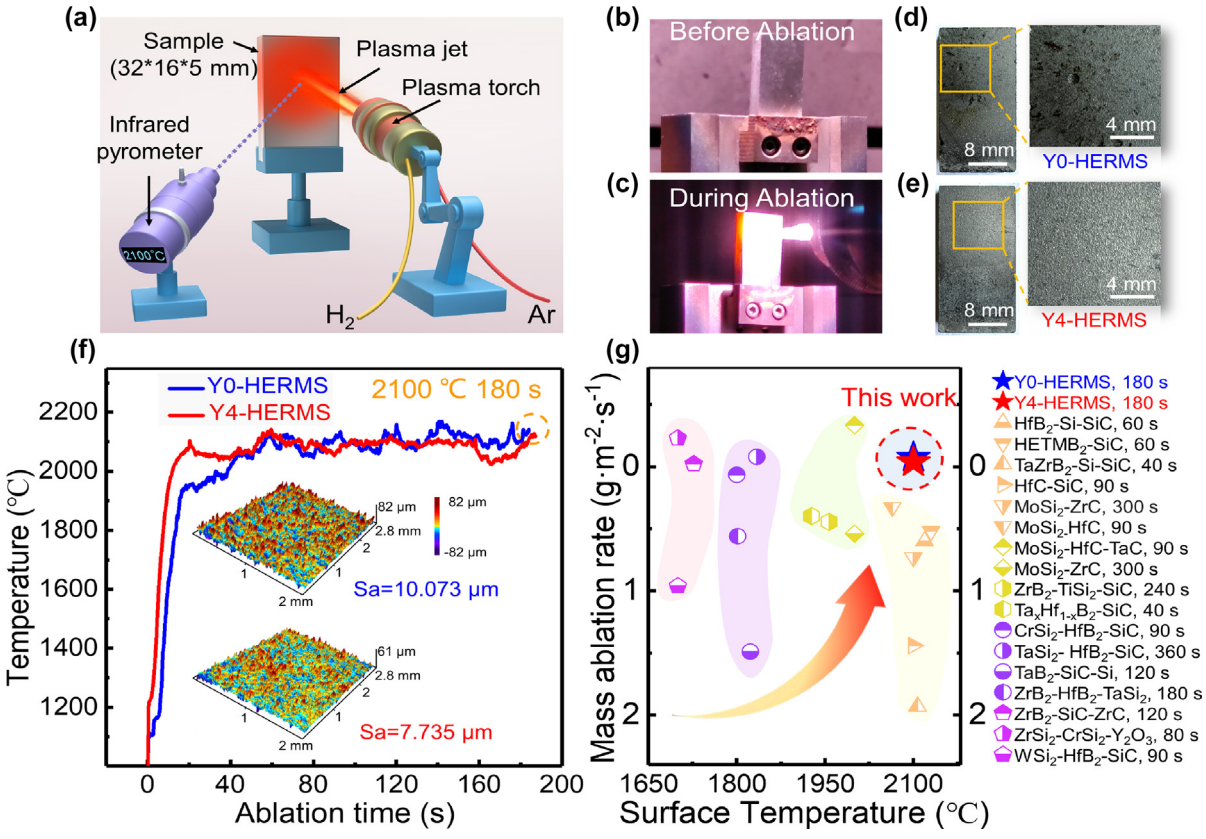

FIG. 1

Ablation performance of high-entropy refractory metal silicide (HERMS) coatings. (a) Schematic diagram of ablation test in the air plasma flame; (b) Macro morphology before ablation; (c) Macro morphology after ablation; Macro morphology of the samples after ablation for 180 s: (d) Y0-HERMS and (e) Y4-HERMS; (f) Surface ablation temperature changed curves of the Y0-HERMS and Y4-HERMS samples and insets are the corresponding 3D morphology and roughness values; (g)Mass ablation rates (MAR) of this work (Y0-HERMS and Y4-HERMS) comparing with a range of candidate silicide coatings[48–63].

Please cite this article in press as: J. Kuang et al., Materials Today (2024), https://doi.org/10.1016/j.mattod.2024.08.012

record the surface temperature of the sample's center zone during ablation, an infrared radiation thermometer was utilized, which was stabilized at specified temperature by adjusting the plasma power supply voltage and current. The linear ablation rate (LAR) and mass ablation rate (MAR) were calculated using the following equations: $LAR=(l_0-l_1)/t$ and $MAR=(m_0-m_1)/(t\cdot S)$, respectively, where m_0, l_0 and m_1, l_1 represent the mass and thickness of specimen before and after ablation respectively, and t is the ablation time.

Characterization methods

The phase composition of the coatings was analyzed by X-ray diffraction (XRD, D8-Discover) using Cu Kα radiation (λ = 1.54 Å). The morphology of the coatings was analyzed using SEM (FEI Nova Nano 450), equipped with an energy dispersive spectrometer (EDS) for elemental analysis. The content and distribution of elements were detected using an electron probe microanalysis system (EPMA, JEOL, JXA-8230). High-resolution transmission electron microscope (HRTEM) images and selected area electron diffraction (SAED) patterns were obtained using an FEI Talos F200X microscope. TEM samples were prepared by focused ion beam (FIB, FEI Quanta 3D) using the in-situ lift-out technique. The 3D surface profile and roughness of the ablated surface were determined using an optical profilometer (Mahr MarSurf LD130). The binding energies of the elements on the surface were investigated using X-ray photoelectron spectroscopy (XPS, Thermo Fisher Nexsa) with an Al Kα (1,486.6 eV) X-ray source. For charge compensation, C 1 s (284.80 eV) was used for calibration.

DFT methods

Spin-polarized density functional theory (DFT) method is utilized to reveal the atomistic mechanisms about the experimental findings in our work by using the Cambridge Sequential Total Energy Package (CASTEP) module in Materials Studio software [30]. Ultrasoft pseudo-potential method is employed to describe the interactions between valence electrons and ionic cores [31]. The generalized gradient approximation method with the Perdew-Burke-Ernzerh function (GGA-PBE) is performed to calculate the exchange and corrections of atomic interaction [32]. A plane-wave basis is set with a cutoff energy of 400 eV and the Brillouin zone is sampled by a Monkhorst-Pack grid [33]. The tolerances of energy, force and displacement for structure optimization are 10^{-6} eV/atom, 0.03 eV/Å and 0.002 Å respectively and the self-consistence field (SCF) is set as 5×10^{-6} eV/atom.

In order to elucidate the effect of yttrium addition on the formation of metal silicide and its anti-oxidative capacity, two sets of models are built. The first set of models is: (1) body-centered cubic NbMoTaW equiatomic RHEA (named as "RHEA" model), (2) RHEA model with surface addition of Y element (named as "RHEA-Ysurf" model), and (3) RHEA model with subsurface addition of Y element (named as "RHEA-Ysub" model). The second set of models is: (1) $(NbMoTaW)Si_2$ with a C40 hexagonal crystal structure (named as "XSi_2" model), (2) XSi_2 model with surface addition of Y element (named as "XSi_2-Ysurf" model), and (3) XSi_2 model with subsurface addition of Y element (named as "XSi_2-Ysub" model). Structure optimization were performed for these two sets of models to optimize the crystal structure, with k points set as $(3 \times 3 \times 2)$. Then the (001) and (0001) surfaces are cleaved from the optimized periodic structures with a vacuum layer of ~15 Å for RHEA and XSi_2 models, respectively. These surface models are geometrically optimized again and utilized to study the effect of Y addition on the formation of metal silicide and its anti-oxidative capacity with k points set as $(3 \times 3 \times 1)$. Specifically, the first set of optimized RHEA surface models are utilized to unveil the effect of Y addition on the formation of metal silicide via the study of their adsorption and diffusion capacity of Si element. The second set of optimized XSi_2 surface models are employed to investigate the effect of Y element in metal silicide on its anti-oxidative capacity via the study of their adsorption and diffusion capacity of O element. Note that vacancy and interstitial diffusion characteristics are assigned to Si diffusion in RHEA models and O diffusion in XSi_2 models, respectively [34,35].

To investigate the adsorption capacity of Si element on different RHEA surfaces, the adsorption energy (E_{ads}^{Si}) is determined by the following equation [36]:

$$E_{ads}^{Si} = E_{RHEA+Si} - E_{RHEA} - E_{Si}$$

where $E_{RHEA+Si}$ and E_{RHEA} are the total energies of the RHEA surface models with and without Si adsorption, respectively. E_{Si} is the energy of a single Si atom.

Similarly, the adsorption capacity of O element on different XSi_2 surfaces can be evaluated with its adsorption energy (E_{ads}^{O}) by using the following equation:

$$E_{ads}^{O} = E_{XSi_2+O} - E_{XSi_2} - E_O$$

where E_{XSi_2+O} and E_{XSi_2} are the total energies of the XSi_2 surface models with and without O adsorption, respectively. E_O is the energy of a single O atom, which is equal to the half of the energy of an O_2 molecule.

The siliconization and oxidation of material surface often occurs from the surface to subsurface, and the diffusion barriers of Si and O atoms are related to the degree of siliconization and oxidation. To investigate the diffusion behaviors of Si and O elements on the surfaces of RHEA and XSi_2 models respectively, a series of intermediate configurations along diffusion paths are produced by interpolating between the structural optimized initial and final configurations, which is geometrically determined using linear synchronous transit (LST) method [37]. The migration energy barriers of Si and O diffusion are determined from the energy difference between transition states (TS) and initial states (IS).

Results and discussion

Ablation performance

The ablation experiment with the air plasma flame was conducted as illustrated by the schematic diagram in Fig. 1a. Fig. 1b and c show photographs of the HERMS sample before and during ablation, respectively. The Y4-HERMS sample, after ablation at 2200 °C for 20 s, effectively retained its original shape, displaying a continuous $Y(Ta_{0.5}Nb_{0.5})O_4$-dispersed SiO_2 structure (Fig. S4 and Fig. S5). In contrast, the Y0-HERMS subjected to the same ablation conditions experienced complete

Please cite this article in press as: J. Kuang et al., Materials Today (2024), https://doi.org/10.1016/j.mattod.2024.08.012

coating destruction, precluding further characterization efforts (Fig. S4 and Fig. S6). To further elucidate the ablation protection mechanism of these coatings, subsequent studies were conducted on samples subjected to an ablation temperature of 2100 °C and an ablation duration of 180 s. The Y0-HERMS surface displays a distinct pattern of ablation spots with a radial distribution, indicating partial melting of the oxide layer (Fig. 1d). In contrast, the Y4-HERMS surface retains shiny appearance with a dense smooth oxide layer (Fig. 1e). 3D surface profiles of the ablation center (Fig. 1f insets) reveal that the roughness of the Y0-HERMS surface (10.073 μm) is 1.3 times higher than that of the Y4-HERMS surface (7.735 μm). This difference is presumably a result of localized melting events within the Y0-HERMS coating, inferred from the formation of oxides observed post-ablation, culminating in an escalated roughness parameter. In contrast, the Y4-HERMS coating demonstrates a remarkable fortitude against ablation-induced degradation, maintaining a surface characterized by minimal damage and a retention of its inherent smooth and shiny appearance. Fig. 1f shows the surface temperature variation curves of the Y0-HERMS and the Y4-HERMS samples during the ablation process, where a surface temperature of 2100 °C is reached over a period of 180 s. Thermal analysis reveals divergent trends in surface temperature between the two coatings; the Y4-HERMS coating achieves a higher degree of thermal stability, in stark contrast to the Y0-HERMS coating, which exhibits more pronounced and frequent thermal fluctuations. Surface temperature is a critical determinant of ablation performance. By combining the surface temperature curves (Fig. 1f) with the ablation morphologies (Fig. 1d and e), it can be inferred that temperature changes, in conjunction with the combined effects of radiation coefficient and relevant chemical reactions, would lead to substantial differences in ablation behavior [38]. Furthermore, the progression of ablation processes exerts a concomitant effect on the thermal profile, indicative of a complex feedback mechanism between thermal behavior and material response. Fig. 1g and Table S1 present a comparison of the ablation resistance between the HERMS coatings and other silicide coatings found in the literature. It is noted that the HERMS coatings endure relatively higher ablation temperatures (2100 °C) and longer protection times (180 s) compared to other silicide coatings (Table S1). Moreover, the MAR for Y0-HERMS is -0.074 g·m^{-2}·s^{-1}, while its LAR is -0.106 μm·s^{-1}. In comparison, Y4-HERMS exhibits the MAR of -0.036 g·m^{-2}·s^{-1} and a LAR of -0.067 μm·s^{-1}. The HERMS coatings exhibit exceptional resistance to high-temperature ablation, as evidenced by their near-zero and negative values for MAR and LAR. The negative ablation rate suggests that controlled oxidation occurs during high-temperature ablation, indicating the formation of a protective oxide layer over the HERMS coatings. This oxide layer effectively shields the underlying samples from further ablation. The near-zero linear ablation rate indicates minimal dimensional changes in the coating under ablative conditions, thus ensuring its structural integrity and preventing significant material loss. This superior performance of the Y4-HERMS coating presumes to be attributed to several factors, including enhanced thermal stability, improved adhesion to the substrate, and heightened resistance to oxidation and ablation (see Protective mechanism section for details).

Microstructure and constituents

The microstructural characteristics and phase composition of the Y0-HERMS and Y4-HERMS samples were elucidated using SEM and XRD analyses. As depicted in Fig. 2a and Fig. S7a, the Y4-HERMS coating is characterized by a homogeneous granular microstructure, with granules averaging 100–200 nm in size. In contrast, the Y0-HERMS coating displays a more heterogeneous grain size distribution, interspersed with smaller, newly formed grains. Cross-sectional morphological analysis, as presented in Fig. 2b and Fig. S7b, was conducted to ascertain the thickness of the coatings. The Y4-HERMS coating exhibited a measured thickness of ~58 μm, which is nearly twice that of the Y0-HERMS counterpart. These results imply that the incorporation of Y notably augments the growth rate of the silicide coating. Fig. 2c presents the phase composition of both Y0-HERMS and Y4-HERMS coatings. The diffraction peaks observed for both coatings reside between the characteristic peaks of $NbSi_2$, $MoSi_2$, $TaSi_2$, and WSi_2, which all crystallize in the $P6_222(180)$ space group, with a near-perfect alignment to the peaks of $NbSi_2$. These observations suggest that the coatings are comprised of a (NbMoTaW)Si_2 solid solution phase, adopting the hexagonal C40-type MSi_2 crystal structure [39]. TEM was utilized to explore the structural characteristics of the Y4-HERMS coating at the substrate interface. As depicted in Fig. 2d, in addition to the primary phase, a distinct secondary phase is observed at the coating-substrate boundary. Fig. S8 shows the elemental distribution across specific local regions of the coating. The Si content within the main phase is similar to that found in the Y0-HERMS coating, with a consistent concentration of ~66 at.% (Fig. S8b). This equates to a silicon-to-metal (Nb, Mo, Ta, and W) atomic percent ratio of 2:1. Concurrently, the secondary phase exhibits a reduced Si content of ~37 at.%, aligning with the characteristics of a low-silicide phase (Fig. S8b). Notably, Y is uniformly dispersed across both phases, with an atomic concentration ranging from 0.5 to 1 percent (Fig. S8c). Fig. 2e and f display the SAED and HRTEM analyses of the two distinct phases, respectively. The phase indicated by the orange box in Fig. 2d is identified as the primary disilicide phase, exhibiting a hexagonal C40-type MSi_2 crystal structure. Conversely, the phase demarcated by the blue box is characterized as a low-silicide phase with a tetragonal M_5Si_3 crystal structure. The formation of the low-silicide phase can likely be ascribed to the enhanced diffusion of Si, induced by the addition of Y during the coating formation.

To elucidate the influence of Y on the formation of silicide coatings, DFT calculations were conducted. Utilizing the elemental composition and crystallographic data derived from our experimental findings, atomistic models of the surface were constructed to assess the impact of Y incorporation on the silicidation process. Fig. S9 shows the geometrically optimized models of the RHEA configurations. These models facilitate an investigation into the role of Y by comparing Si adsorption and diffusion across three distinct scenarios: 1) without Y addition (Fig. S9a and d), 2) with surface addition of Y (Fig. S9b and e), and 3) with subsurface addition of Y (Fig. S9c and f). As shown in Fig. S10, it is demonstrated that Si atom prefers to stabilize at the hollow sites surrounded by metal atoms. The introduction of Y element at the surface (RHEA-Ysurf model) or at the subsurface (RHEA-

Please cite this article in press as: J. Kuang et al., Materials Today (2024), https://doi.org/10.1016/j.mattod.2024.08.012

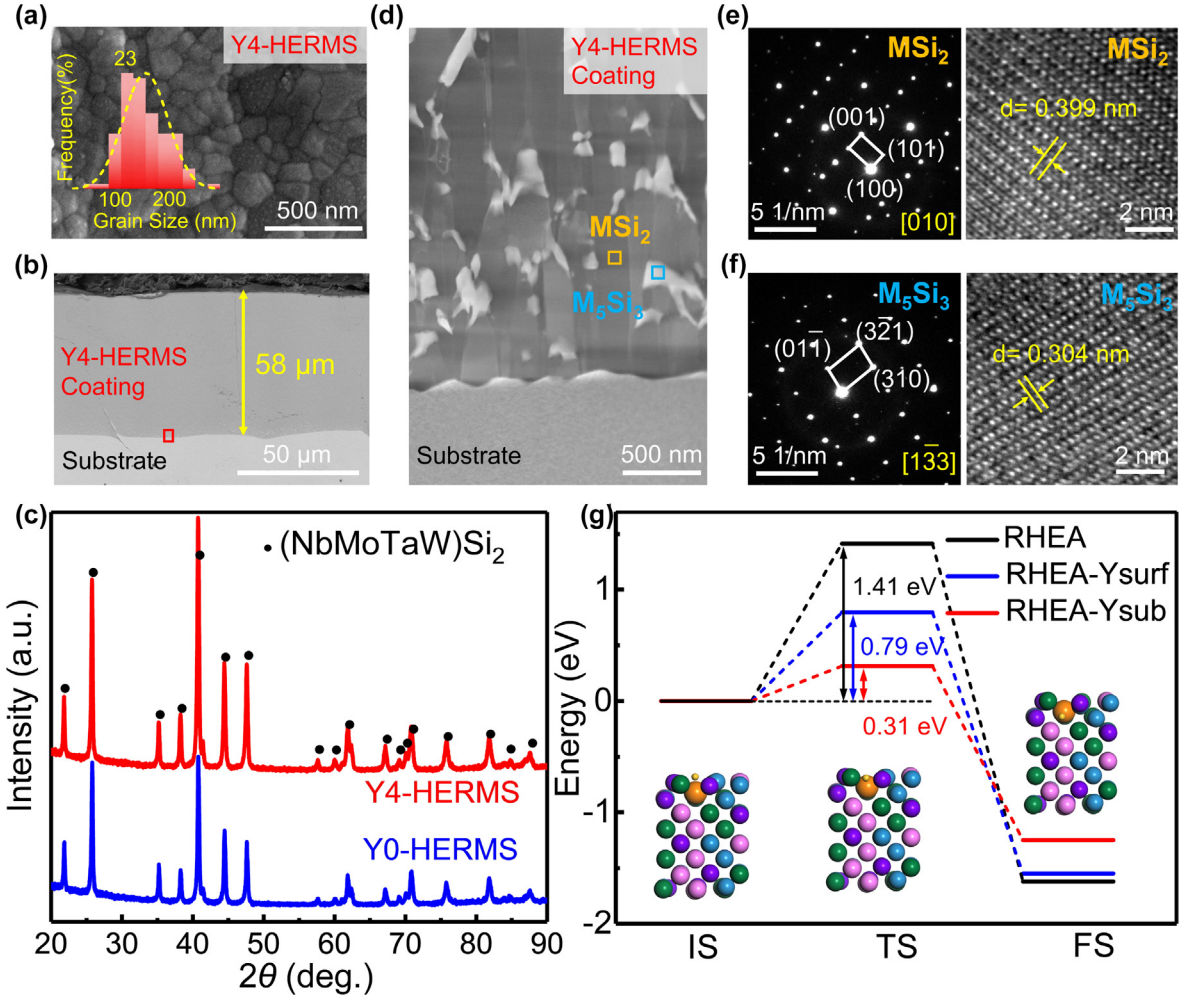

FIG. 2

Microstructure and constituents of the HERMS coatings. (a) Surface SEM image of Y4-HERMS coating and inset is size distribution of grains; (b) Cross-section morphology of Y4-HERMS coating; (c) XRD results of Y0-HERMS and Y4-HERMS coatings; (d) STEM image of the interface between Y4-HERMS coating and substrate; (e)SAED and HRTEM image of orange box in (d); (f)SAED and HRTEM image of blue box in (d); (g) Energy diagrams and the IS, TS and FS configurations of Si diffusing from surface to subsurface of the RHEA models. The IS, TS, FS are initial state, transition state and final state, respectively.

Ysub model) only slightly reduces the Si adsorption energies (Fig. S11), which indicates that the accelerated formation of metal silicide does not originate from Si adsorption affected by Y addition. However, the energy barrier of Si diffusing into RHEA subsurface is 1.41 eV for the model without Y addition, while the energy barriers for RHEA-Ysurf and RHEA-Ysub models are 0.79 and 0.31 eV, respectively (Fig. 2g). The significant reduction in energy barriers for Si diffusion, facilitated by the surface or subsurface addition of Y, indicates that Y addition can significantly promote Si diffusion along the vacancy sites in the high-entropy NbMoTaW alloy. Particularly, subsurface addition of Y element proves to be particularly advantageous in promoting the formation of (NbMoTaW)Si_2. This observation is significant given that a sufficient thickness of the coating is critical to ensure robust ablative resistance over extended periods.

Protective mechanism

Fig. 3 presents the microstructure and composition of the Y4-HERMS coating following ablation. Post-ablation, the surface of the Y4-HERMS coating demonstrates a relatively dense structure interspersed with a significant number of Y-rich particles, as shown in Fig. 3a. To elucidate the ablation mechanism operative in the HERMS coatings, it is imperative to conduct a comprehensive analysis of the structural characteristics within the oxide layer. To facilitate this analysis, thin cross-sectional samples were lifted from the surface of the ablated coatings utilizing FIB technique. These samples were subsequently examined using TEM coupled with EDS, to provide detailed insights into the microstructural and compositional changes induced by ablation. As shown in Fig. 3b, the oxide layer of the Y4-HERMS exhibits a thickness of ~2 μm and consists of a single-layer structure. Within the oxide layer, Y-containing particles (red square in Fig. 3b) with nanoscale and microscale skeleton structure ranging in size from 100 nm to 2 μm are dispersed throughout an amorphous SiO_2 matrix (yellow square in Fig. 3b), which are evidenced by SAED patterns and HRTEM images (Fig. 3c–f). The amorphous nature of the SiO_2 can be attributed to its rapid cooling from the peak temperature of 2100 °C at the center of the

Please cite this article in press as: J. Kuang et al., Materials Today (2024), https://doi.org/10.1016/j.mattod.2024.08.012

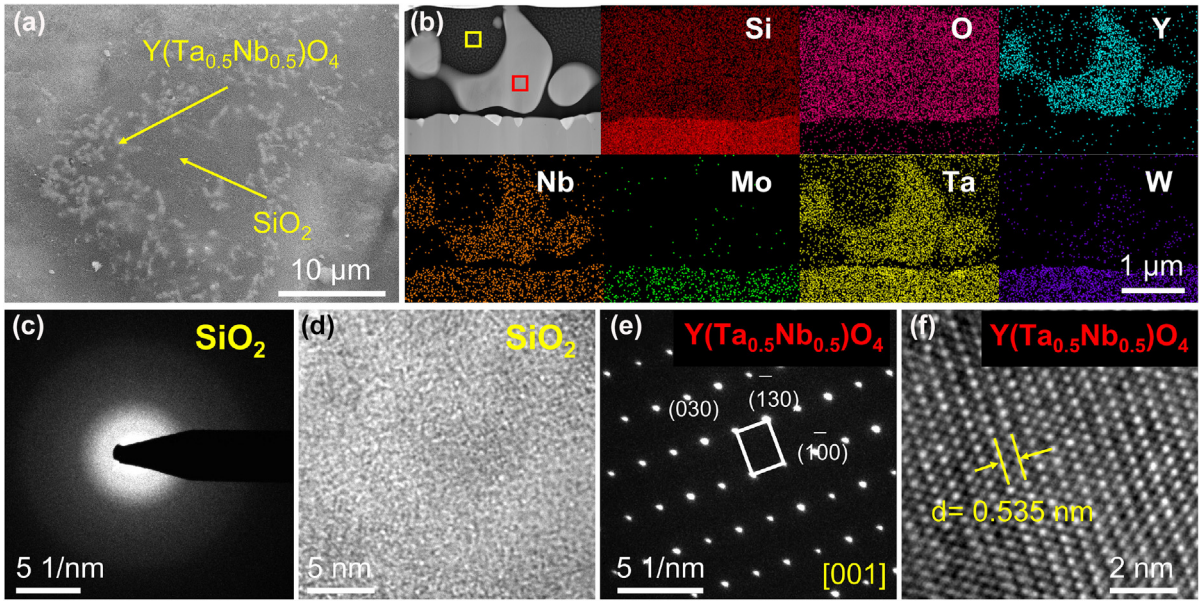

FIG. 3

Microstructure and constituent of the HERMS coatings after ablation. (a)Surface SEM image of Y4-HERMS coating sample after ablation; (b) Cross-section STEM image and EDS mapping images of Y4-HERMS coating after ablation; (c)SAED of yellow box in (b); (d) HRTEM image of yellow box in (b); (e)SAED of red box in (b); (f) HRTEM image of red box in (b).

sample surface to room temperature within a few minutes, which inhibits its crystallization process [29]. EDS analysis reveals that these particles predominantly contain Y, Ta, Nb and O (Fig. S12). Furthermore, the SAED pattern and HRTEM analysis (Fig. 3e and f) suggest that these particles exhibit a monoclinic crystal structure, corresponding to $Y(Ta_{0.5}Nb_{0.5})O_4$. During ablation, the MoO_3 and WO_3 are characterized by high Gibbs free energy and exhibit substantial volatility, leading to their preferential evaporation. Consequently, the residual oxide layer is predominantly enriched with Y, Ta, Nb, Si, and O. As the system cools, a reaction between Y_2O_3 and Ta_2O_5 leads to the formation of $YTaO_4$ within the oxide layer. In parallel, $YNbO_4$ is also generated. These oxides have the capacity to form a solid-solution phase, denoted as $Y(Ta_{0.5}Nb_{0.5})O_4$, which subsequently precipitates from the SiO_2 matrix. The precipitation of $Y(Ta_{0.5}Nb_{0.5})O_4$ gives rise to a composite oxide layer structure featuring both nanoscale and microscale skeleton morphology. Moreover, the $(Nb,Mo,Ta,W)_5Si_3$ phase appears at the interface in the silicide layer (Fig. S13). This low silicon phase is likely the result of chemical reactions and diffusion processes occurring at the interface. During the ablation process, Si preferentially forms SiO_2, leading to continuous consumption of Si in the silicide layer and resulting in the formation of $(Nb,Mo,Ta,W)_5Si_3$. To further confirm the phase composition of the Y4-HERMS coating after ablation, XPS analysis of the oxidation products in the central area was performed. Particularly, Fig. S14a shows that Si 2p XPS spectra for the Y4-HERMS coating before ablation. It appears two peaks at binding energies of 102.40 eV and 99.85 eV, which were assigned to the Si-M (M=Nb, Mo, Ta, W) bonds (102.40 eV) deriving from the $(NbMoTaW)Si_2$ and zero-valent Si (Si^0, 99.85 eV), respectively, which is owing to the decomposition of Si during pack cementation [40–43]. After ablation, a primary peak corresponding to SiO_2 bonds can be found, which is attributed to the ablation of Y4-HERMS coating. It is well known that Y 3d XPS region is overlapping with that of Si 2 s. The XPS spectra of Si 2 s (Fig. S14b) also demonstrates that unablated coating is composed of Si-M bonds and Si matrix, while the oxidized coating is composed of SiO_2. Obviously, the Y 3d XPS spectrum of the ablated coating exhibits peaks at 160.7 eV and 158.7 eV, corresponding to Y 3d3/2 and Y 3d5/2, respectively, consistent with Y^{3+}oxidation state [44,45]. Additionally, post-ablation surface analysis of the Y4-HERMS coating reveals the presence of various metal oxides (Nb_2O_5, MoO_3, Ta_2O_5, WO_3), along with a notable reduction in the relative strength of M−Si bonds [46] (Fig. S14c–f). Combining with the EDS results in Fig. S12, the TEM results in Fig. 3 and the possible oxidation reactions involving stable ablated species (Y_2O_3, Ta_2O_5, and Nb_2O_5), the formation of $Y(Ta_{0.5}Nb_{0.5})O_4$ during ablation is confirmed.

As contrast, a representative center region on the surface of the Y0-HERMS coating after ablation is shown in Fig. S15. The surface morphology exhibits numerous holes, which may be attributed to partial evaporation of the low melting point oxide during the ablation process at 2100 °C. Fig. S16 shows that the oxide layer of the Y0-HERMS displays a thickness of ~1 μm and consists of a dual-layer structure comprising a porous outer layer and a dense inner layer. As shown in Fig. S17a and b, it has been determined that both the outer and inner oxide layers are composed of SiO_2. The presence of the porous and loose structure in the outer layer can be attributed to the release of volatile species or the diffusion of gaseous by-products from the oxide layer. The porosity facilitates the penetration behavior to the material, thereby compromising the integrity of the oxide layer and diminishing its protective capabilities. However, the inner oxide layer exhibits a strong bond with the silicide layer

Please cite this article in press as: J. Kuang et al., Materials Today (2024), https://doi.org/10.1016/j.mattod.2024.08.012

and shows no signs of delamination. As depicted in Fig. S17c–f, similar to the Y4-HERMS sample, the silicide layer exhibits two phases, containing the primary $(NbMoTaW)Si_2$ ($HEMSi_2$ for short) phase and secondary $(Nb,Mo,Ta,W)_5Si_3$ (HEM_5Si_3 for short) phase. Furthermore, the extent of the coating degradation post-ablation is a critical determinant of its ablative resistance. Cross-sectional SEM of the HERMS coatings (Fig. 4a and b) and EPMA of the Y4-HERMS sample (Fig. S18) reveal that the ablated coating is composed of a tri-layered architecture. This structure encompasses a surface oxidation layer, an intermediate silicide layer, and a diffusion layer beneath. The integrity and interfacial stability of these layers are imperative for the coating's ability to resist ablation. The presence of the low-silicon diffusion layer is attributed to the difference in Si concentration between the silicide layer and the substrate, leading to inevitable interdiffusion between Si and the alloy elements (Nb, Mo, Ta, W) at high temperature during ablation process. The occurrence of the diffusion layer reflects the degradation of the silicide coating, resulting in a reduction of available Si for SiO_2 formation during ablation. Comparative analysis of the two HERMS coatings reveals a marked difference in the diffusion layer thicknesses: the Y0-HERMS coating exhibits a diffusion layer of ~14 μm, whereas the Y4-HERMS coating demonstrates a considerably reduced thickness of 4 μm. This significant reduction in the diffusion layer thickness of the Y4-HERMS coating with sluggish diffusion effect caused by the high-entropy single-phase structure implies enhanced thermal stability and a lower propensity for interdiffusion at elevated temperatures. Consequently, these attributes are indicative of an improved ablation resistance performance for the Y4-HERMS coating. Fig. S19 shows the TEM analysis of the two-phase region at the interface between the silicide layer and the diffusion layer, revealing consistent structures in both HERMS coatings. It is observed that the grain size of the low-silicon phase in the Y4-HERMS coating is smaller than that of the Y0-HERMS coating, indicating that the presence of Y not only refines the silicide but also contributes to the refinement of the low-silicon phase. Fig. 4c displays the schematic diagram for the ablation behavior of the HERMS coatings. During the high-temperature ablation process, the Y4-HERMS coating experiences intense heat fluxes, leading to the formation of oxide layer on the surface. The presence of Y, Ta, and Nb within the oxide layer facilitates the formation of $Y(Ta_{0.5}Nb_{0.5})O_4$, which offers superior thermal stability and resistance to thermal shock. It was reported that the $Y(Ta_{0.5}Nb_{0.5})O_4$ particles act as sacrificial agents, absorbing and dissipating the thermal energy by undergoing the tetragonal-monoclinic (t-m) phase transition during ablation, which prevents excessive heat from propagating further into the substrate or underlying coating layers[47]. Moreover, the nanocrystalline and skeleton structures of $Y(Ta_{0.5}Nb_{0.5})O_4$ within the SiO_2 matrix further prevent the evaporation of the SiO_2 and the viscosity of the oxide layer. Thus, the oxide layer possesses excellent structural stability and protects the sample from further ablation damage. However, for Y0-HERMS coating, the presence of a large amount of gas during the ablation process leads to numerous voids in the oxide film which deteriorates its ablative resistance.

To further reveal the protective mechanisms, we also analyzed the O adsorption and diffusion of three XSi_2 models: 1) without Y addition, 2) with surface addition of Y, and 3) with subsurface addition of Y. The effect of Y addition on the ablative ability of the HERMS is also studied. The geometrically optimized XSi_2 configurations are shown in Fig. S20 The O adsorption capacity at a series of bridge sites of $(NbMoTaW)Si_2$ surfaces are investigated, taking the effect of Y element into account (Fig. S21). It can be observed that bridge sites exhibit strong O adsorption capacity (Fig. S22). More importantly, our experimental findings

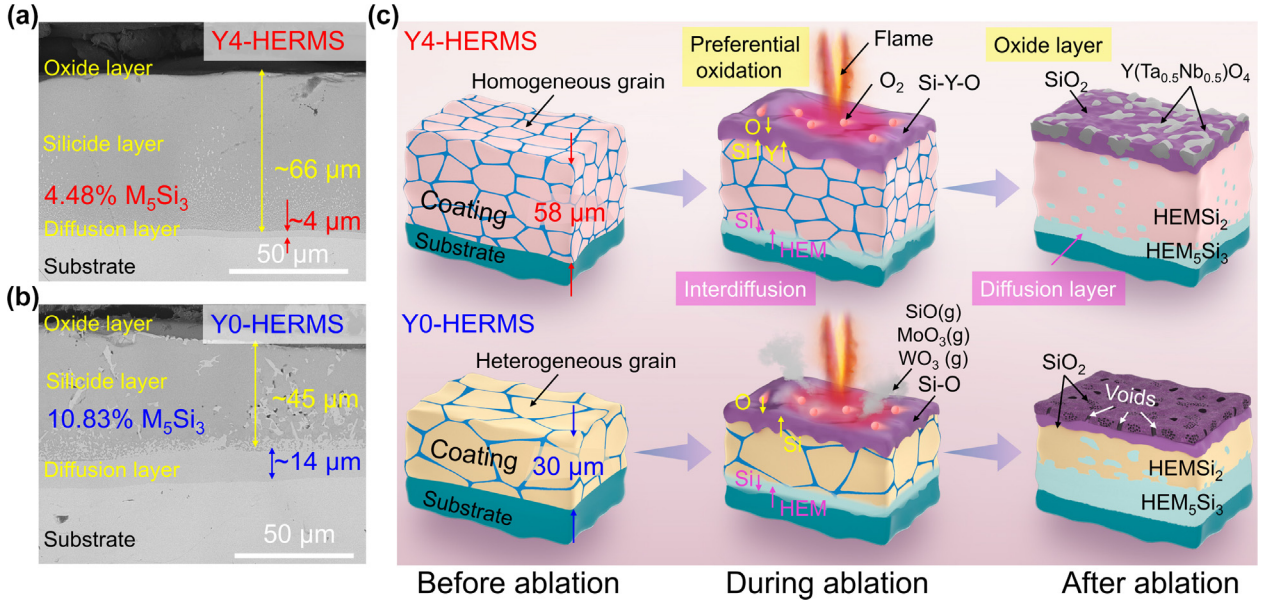

FIG. 4

Cross-section microstructure evolution of the HERMS coatings during ablation. Cross-section SEM images of samples after ablation: (a) Y4-HERMS and (b) Y0-HERMS; (c) Schematic diagram of the cross-sectional microstructure evolution of the HERMS coatings during ablation at 2100 °C for 180 s.

Please cite this article in press as: J. Kuang et al., Materials Today (2024), https://doi.org/10.1016/j.mattod.2024.08.012

demonstrated that the Si element in (NbMoTaW)Si_2 can be oxidized most easily which promotes the formation of an antioxidant SiO_2 layer. Therefore, the interaction intensity between O and Si element is further explored. The analysis of electron density difference demonstrated that the electron gain of O atom from Si element is more significant than metal atoms (Fig. 5a), in which the electron gain of O atom from Si atom in Ysurf-Si site is most remarkable. The difference of Si-O bonding distance at W-Si, W-Si with Y substitution (W-Si(Ysub)) and Ysurf-Si sites is also consistent with the divergence of interaction density between O and Si atoms. It can be found that Y element enhance the Si-O bond strength, which will increase the viscosity of SiO_2. Partial density of states (PDOS) of W/Y, Si and absorbed O atoms after O adsorption at W-Si, Ysurf-Si and W-Si (Ysub) sites is also analyzed (Fig. 5b and Fig. S23). The interaction between O atom with metal elements is weaker than that with Si element for all these bridge sites. Besides, O atom strongly interacts with W and Si at W-Si site while its interaction with Y is very weak accompanied by enhanced interaction with Si at Ysurf-Si site. Comparative analysis of the PDOS for W-Si and W-Si (Ysub) sites indicates a discernible alteration in electronic interactions. The incorporation of Y in the W-Si coordination environment appears to attenuate the bonding between Si atoms and adsorbed O, potentially inhibiting the formation of SiO_2. From these observations, it can be deduced that within the (NbMoTaW)Si_2 complex, Si is the most susceptible to oxidation. It is proposed that Y atoms situated at the surface can facilitate the formation of a SiO_2 layer. Conversely, Y atoms positioned in subsurface locations lack this promotive effect on the SiO_2 layer formation. On the other hand, the energy barrier of O diffusing into the subsurface of XSi_2 model is 5.04 eV, while the O diffusion energy barriers in XSi_2-Ysurf and XSi_2-Ysub models are 6.27 and 6.30 eV, respectively (Fig. 5c). The increased energy barriers for O diffusion by surface or subsurface addition of Y element indicate that Y addition can retard O diffusion into metal silicide layer, which could also account for the improved anti-oxidation capacity in addition to the formation of antioxidant SiO_2 layer.

Conclusions

In summary, this study represents a significant breakthrough in materials engineering for high-temperature applications. We have successfully developed a novel yttrium-modified high-entropy silicide coating on a NbMoTaW alloy. This advancement was achieved through mechanisms of solid solution formation and atomic diffusion facilitated by the HAPC process. The inclusion of Y has been found to markedly facilitate Si diffusion, leading to increased coating thickness and a refined microstructure of the grains. Notably, the Y4-HERMS coating owing to sluggish dif-

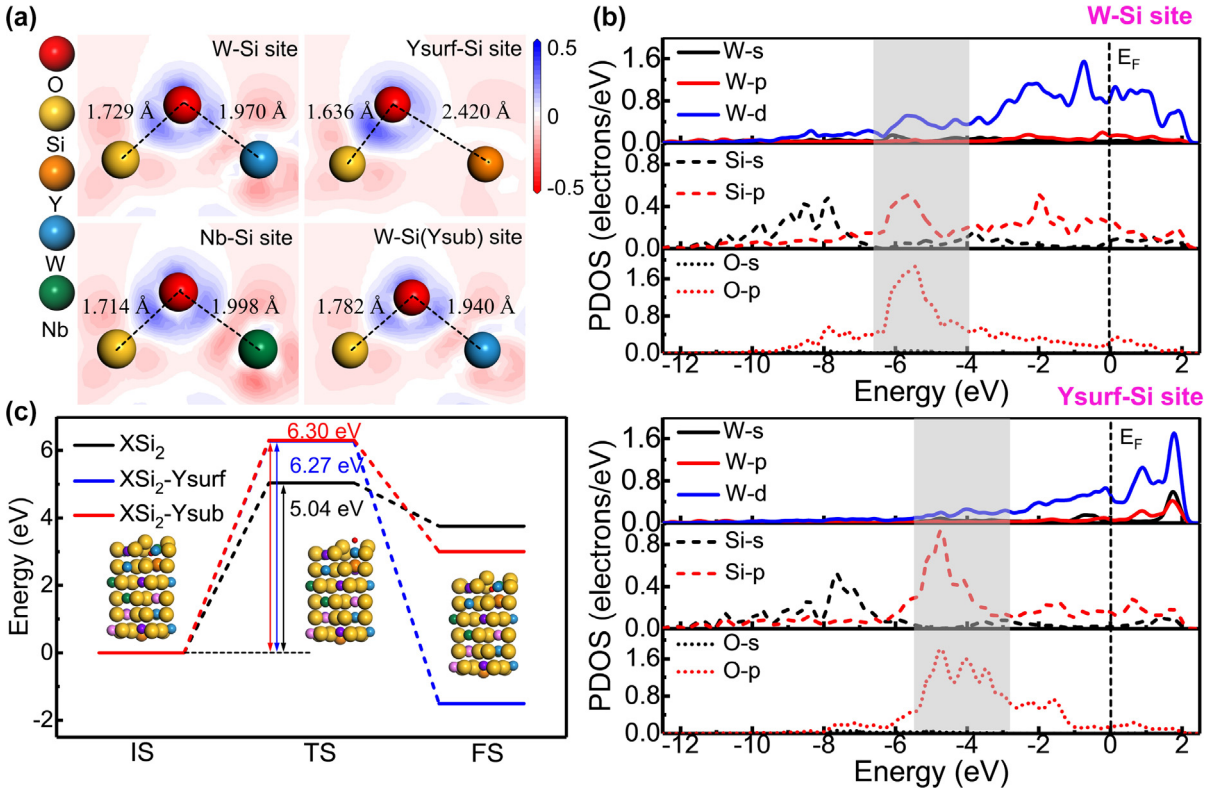

FIG. 5

DFT of O absorption and diffusion in HERMS coating. (a) DFT simulation results of 2D electron density difference and bonding distance between the absorbed O atom and the W-Si, Ysurf-Si, Nb-Si and W-Si(Ysub) bridge sites after O adsorption onto the surface of XSi_2 models. Red and blue represent the depletion and accumulation of electrons with the unit of e·Å^{-3}, respectively; (b) Partial density of states (PDOS) of W, Si and absorbed O atoms after O adsorption at W-Si site and Ysurf-Si site. The shaded area highlights the region showing a significant electron interaction between absorbed O atom and W-Si bridge site. The black dashed lines at the energy of zero indicate the Fermi level (E_F). (c) Energy diagrams and the IS, TS and FS configurations of O diffusing from surface to subsurface of the XSi_2 models.

Please cite this article in press as: J. Kuang et al., Materials Today (2024), https://doi.org/10.1016/j.mattod.2024.08.012

fusion effect exhibits exceptional anti-ablation performance at 2100 °C for 180 s, displaying negligible signs of ablation damage. Moreover, the in-situ formation of $Y(Nb_{0.5}Ta_{0.5})O_4$ as skeletal architecture within intact Si-Y-O oxide layer also emerges as a pivotal factor, enhancing the thermal stability and ablation resistance of the SiO_2 scale. Theoretical insights from DFT calculations elucidate that the inclusion of Y within the HERMS coating significantly influences the ablation resistance characteristics. The role of Y addition is multifaceted: it promotes the formation of SiO_2, strengthens the Si-O bonds, increases the viscosity of the SiO_2 layer, and impedes the diffusion of O into the metal silicide layer, contributing collectively to the superior ablation resistance of the coating. Furthermore, the findings furnish valuable insights into the evolution of the oxide layer and the underlying ablation resistance mechanisms characteristic of the HERMS coating. Consequently, the deployment of high-entropy refractory metal silicide coatings substantially broadens the operational scope of RHEAs, offering a promising avenue for their application in extreme environments where ablative endurance is paramount.

Author contributions

B.L.S., P.Z., X.B.L., and Y.L. designed the research; J.K., G.M.Y., B. S., Y.X., and Y.Y.Y. prepared and characterized the samples; L.G. S. carried out DFT simulations; J.K., Z.J., Q.Q.W., P.F.H., Y.L., and B.L.S. analyzed the data and discussed the results; J.K., Z.J., and L. G.S. wrote the manuscript. All authors reviewed and contributed to the final manuscript.

CRediT authorship contribution statement

Juan Kuang: Writing – review & editing, Writing – original draft, Visualization, Methodology, Investigation, Data curation. **Qianqian Wang:** Writing – review & editing, Supervision, Data curation. **Zhe Jia:** Writing – review & editing, Writing – original draft, Visualization, Funding acquisition. **Guoming Yi:** Writing – review & editing, Methodology. **Bo Sun:** Methodology, Investigation. **Yiyuan Yang:** Writing – review & editing, Formal analysis. **Ligang Sun:** Writing – review & editing, Writing – original draft, Software, Resources. **Ping Zhang:** Writing – review & editing, Investigation, Conceptualization. **Pengfei He:** Methodology, Formal analysis. **Yue Xing:** Validation. **Xiubing Liang:** Writing – review & editing, Resources, Project administration. **Yang Lu:** Writing – review & editing, Visualization, Conceptualization. **Baolong Shen:** Writing – review & editing, Supervision, Project administration, Funding acquisition, Conceptualization.

Data availability

Data will be made available on request.

Declaration of competing interest

The authors declare that they have no known competing financial interests or personal relationships that could have appeared to influence the work reported in this paper.

Acknowledgements

This work is supported by the National Natural Science Foundation of China (52231005, 52201174), the Jiangsu Provincial Key Research and Development Program (BE2021088), Natural Science Foundation of Jiangsu Province (BK20220858), the Fundamental Research Funds for the Central Universities (2242023K40029), the Opening Project of Jiangsu Key Laboratory of Advanced Structural Materials and Application Technology (ASMA202302), Guangdong Basic and Applied Basic Research Foundation (2020A1515110236, 2022A1515011402) and Science, Technology, and Innovation Commission of Shenzhen Municipality (ZDSYS20210616110000001).

Appendix A. Supplementary material

Supplementary data to this article can be found online at https://doi.org/10.1016/j.mattod.2024.08.012.

References

[1] Y. Zeng et al., Nat. Commun. 8 (2017) 15836.
[2] A.B. Peters et al., Nat. Commun. 15 (2024) 3328.
[3] S. Chen et al., Mater. Today 65 (2023) 14–25.
[4] Z. Wang et al., Mater. Today 54 (2022) 83–89.
[5] R. Su et al., Acta Mater. 246 (2023) 118719.
[6] S. Sheikh et al., Intermetallics 123 (2020) 106838.
[7] Z. Wen et al., Corros. Sci. 207 (2022) 110574.
[8] Y. Zhang et al., Corros. Sci. 195 (2022) 109977.
[9] G. Yue et al., J. Alloys Compd. 870 (2021) 159498.
[10] L. Zhou et al., J. Mater. Sci. Technol. 111 (2022) 88–98.
[11] C. Wang et al., Corros. Sci. 163 (2020) 108249.
[12] L. Xiao et al., Corros. Sci. 173 (2020) 108751.
[13] Z. Yi et al., Ceram. Int. 48 (2022) 9848–9857.
[14] P. Zhang, X. Guo, Corros. Sci. 53 (2011) 4291–4299.
[15] R. Su et al., Corros. Sci. 221 (2023) 111365.
[16] X. Tian, X. Guo, Surf. Coat. Technol. 204 (2009) 313–318.
[17] C.C. Wang et al., J. Eur. Ceram. Soc. 40 (2020) 4419–4427.
[18] J. Ma et al., Corros. Sci. 209 (2022) 110802.
[19] D. Liu et al., Mater. Lett. 268 (2020) 127629.
[20] Y. Qin et al., J. Eur. Ceram. Soc. 40 (2020) 2752–2759.
[21] A. Ostovari Moghaddam et al., J. Alloys Compd. 927 (2022) 167102.
[22] A. Salian et al., Int. J. Appl. Ceram. Technol. 20 (2023) 2635–2660.
[23] J. Song et al., J. Mater. Sci. Technol. 136 (2023) 149–158.
[24] Z. Tang et al., Adv. Funct. Mater. 34 (2024) 2312239.
[25] L. Liu et al., Scripta Mater. 189 (2020) 25–29.
[26] S. Ye et al., J. Eur. Ceram. Soc. 42 (2022) 5314–5322.
[27] J. Kuang et al., Corros. Sci. 198 (2022) 110134.
[28] G. Yi et al., J. Alloys Compd. 916 (2022) 165384.
[29] B. Chen et al., Adv. Sci. 10 (2023) 2304254.
[30] S.J. Clark et al., Z. Kristallogr. 220 (2005) 567–570.
[31] D. Vanderbilt, Phys. Rev. B 41 (1990) 7892–7895.
[32] J.P. Perdew et al., Phys. Rev. Lett. 77 (1996) 3865–3868.
[33] H.J. Monkhorst, J.D. Pack, Phys. Rev. B 13 (1976) 5188–5192.
[34] S. Zhang et al., J. Mater. Sci. Technol. 115 (2022) 103–114.
[35] H. Xing et al., J. Mater. Sci. Technol. 62 (2021) 180–194.
[36] E.d.V. Gómez et al., Appl. Surf. Sci. 420 (2017) 1–8.
[37] T.A. Halgren, W.N. Lipscomb, Chem. Phys. Lett. 49 (1977) 225–232.
[38] X. Xu et al., Corros. Sci. 192 (2021) 109814.
[39] J. Gild et al., J. Materiomics 5 (2019) 337–343.
[40] C.-C. Wang et al., Ceram. Int. 46 (2020) 6723–6732.
[41] A. Fissel et al., J. Appl. Phys. 99 (2006) 074105.
[42] H. Kato et al., J. Vac. Sci. Technol., A 24 (2006) 1505–1508.
[43] T. Yang, X. Guo, Int. J. Refract. Met. Hard Mater. 88 (2020) 105200.
[44] L.L. Noto et al., J. Lumin. 140 (2013) 14–20.
[45] X. Wang et al., J. Alloys Compd. 474 (2009) 499–504.
[46] C. Wang et al., Compos. Part b: Eng. 125 (2017) 181–194.
[47] C. Qu et al., J. Am. Ceram. Soc. 106 (2022) 2476–2490.
[48] P. Zhang et al., J. Eur. Ceram. Soc. 41 (2021) 6223–6237.
[49] P. Zhang et al., Ceram. Int. 48 (2022) 12608–12624.
[50] Y. Jiang et al., Ceram. Int. 47 (2021) 11358–11371.

Please cite this article in press as: J. Kuang et al., Materials Today (2024), https://doi.org/10.1016/j.mattod.2024.08.012

[51] T. Liu et al., Ceram. Int. 44 (2018) 8946–8954.
[52] R. Chen et al., Corros. Sci. 205 (2022) 110418.
[53] K. Shuai et al., Corros. Sci. 193 (2021) 109884.
[54] J. Li et al., J. Alloys Compd. 824 (2020) 153934.
[55] X. Ren et al., Corros. Sci. 87 (2014) 479–488.
[56] P. Wang et al., Corros. Sci. 167 (2020) 108536.
[57] Y. Jiang et al., Ceram. Int. 45 (2019) 6541–6551.
[58] Y. Wang et al., Surf. Coat. Technol. 466 (2023) 129615.
[59] Y. Zhang et al., Ceram. Int. 44 (2018) 3056–3063.
[60] F. Liu et al., Ceram. Int. 47 (2021) 15030–15038.
[61] P. Wang et al., Corros. Sci. 177 (2020) 108964.
[62] J. Zhang et al., J. Am. Ceram. Soc. 107 (2024) 461–474.
[63] J. Zhang et al., Corros. Sci. 192 (2021) 109853.

Please cite this article in press as: J. Kuang et al., Materials Today (2024), https://doi.org/10.1016/j.mattod.2024.08.012